Evidence for new crystalline phases formed during early stages of crystallization of amorphous FeCuNbSiB alloys

2006 J. Phys.: Condens. Matter 18 6607

(http://iopscience.iop.org/0953-8984/18/29/004)

INSTITUTE OF PHYSICS PUBLISHING JOURNAL OF PHYSICS: CONDENSED MATTER

J. Phys.: Condens. Matter **18** (2006) 6607–6620 doi:10.1088/0953-8984/18/29/004

Evidence for new crystalline phases formed during early stages of crystallization of amorphous FeCuNbSiB alloys

G A Basheed, S Sarkar and S N Kaul

School of Physics, University of Hyderabad, Central University PO, Hyderabad-500 046, Andhra Pradesh, India

E-mail: kaulsp@uohyd.ernet.in

Received 6 March 2006
Published 30 June 2006
Online at stacks.iop.org/JPhysCM/18/6607

Abstract

Amorphous FeCuNbSiB alloys with composition near $Fe_{73.5}Cu_1Nb_3Si_{13.5}B_9$ (the well-studied FINEMET alloy) were annealed at 520 °C for different durations of time, t_A, varying from 3 to 20 min. Detailed investigation of the structure and composition of crystalline phases formed during the initial stages of crystallization in these alloys using techniques such as x-ray diffraction, Mössbauer spectroscopy, scanning electron microscopy, atomic force microscopy and energy dispersive absorption of x-rays, revealed the following. New crystalline phases, tetragonal Fe_3B and hexagonal Fe_2Si, not reported previously, exist in all the nanocrystalline alloys in question in contrast to the well-documented cubic Fe–Si phase with the DO_3 structure which coexists with the Fe_3B and Fe_2Si phases in some compositions only. The crystallization of Fe_3B and Fe_2Si nanocrystalline grains starts at the surface of the ribbons and then proceeds to the bulk whereas the crystallization of DO_3 Fe–Si gets initiated within the bulk. The average size of the nanocrystalline grains of the Fe_3B and Fe_2Si and cubic DO_3 Fe–Si structures in the residual amorphous matrix is around 20 nm but their volume fractions are as low as ≈5%, 10%, and 7%, respectively. The cubic Fe–Si nanocrystals of the DO_3 structure have a silicon concentration in the range 15–20 at.%. The magnetic moments in the amorphous precursor point, on average, are 40° out of the ribbon plane while in the nanocrystalline alloys this angle varies between 2° and 19° depending on the Fe concentration.

1. Introduction

The discovery [1] of unusual soft magnetic properties (i.e., a unique combination of large saturation magnetization, very low coercivity and high magnetic permeability) in a partially

devitrified amorphous alloy of composition $Fe_{73.5}Cu_1Nb_3Si_{13.5}B_9$, in which ultrafine crystalline grains of mean size 10 nm (called nanocrystalline grains) are embedded in a residual amorphous matrix, has generated enormous interest [2–26] in the study of nanocrystalline alloys with the same or similar composition. Magnetic softening in these alloys, commercially known as FINEMET, is essentially due to the averaging out of the local magneto-crystalline anisotropy of individual nanocrystalline grains over the exchange correlated volume by the exchange interactions that couple nanocrystalline grains through the spins constituting the amorphous matrix. The magnetic properties are thus expected to be extremely sensitive to (i) the size and crystallographic structure of nanocrystalline grains, (ii) the crystalline volume fraction, (iii) the nature of the interfaces between nanocrystalline grains and the amorphous matrix, and (iv) the composition of the residual amorphous matrix. This realization has motivated detailed investigations of the crystallographic structure and composition of the nanocrystalline phases in amorphous $Fe_{73.5}Cu_1Nb_3Si_{22.5-x}B_x$ ($5 \leqslant x \leqslant 12$) alloys annealed for time durations $t_A \leqslant 1$ h at temperatures typically in the range $480\,^{\circ}C \leqslant T_A \leqslant 600\,^{\circ}C$. In this range of annealing temperatures, T_A, and time durations, t_A, there seems to be a broad consensus on the presence of residual amorphous phase and nanocrystalline Fe–Si grains of mean size [3, 8, 10] 10–20 nm that have the DO_3 structure [5–11, 16–21] and a silicon content of 16–22 (at.%), based on the results of phase analysis of the most extensively studied nanocrystalline alloy with $x = 9$. However, there are reports of bcc Fe–Si nanocrystalline phase [2, 4, 14] or DO_3 nanocrystalline phase occasionally accompanied by [7] nanocrystalline grains of the tetragonal Fe_3B structure. For $T_A > 600\,^{\circ}C$ and $t_A \geqslant 1$ h, there is a complete agreement with regard to the presence of DO_3 Fe–Si phase but opinions differ about the existence of additional nanocrystalline phases, e.g., Fe_2B [22], Fe_3B [7], $Fe_3(Si, B)$ [6], $Fe_{23}B_6$ [8], $(Fe, Si)_3B$ [9], Fe_2B and Fe_3B [5], and $Fe_{23}B_6$ and Fe_2B [23, 24]. The presence of Fe–B phases is detrimental [27, 28] to the soft magnetic properties because of larger magneto-crystalline anisotropy.

In view of the sensitivity of soft magnetic properties to the composition and the structure of nanocrystalline grains, a serious discrepancy between the results of structural investigations on FINEMET, particularly in the initial stages of crystallization, calls for a more intensive study. The present work attempts to tackle this issue by exploring the possibility that the disparity in question arises from the use of amorphous precursor samples, in previous investigations, whose actual composition deviates from the nominal composition $Fe_{73.5}Cu_1Nb_3Si_{13.5}B_9$ by varying amounts. For this reason, amorphous alloys in which the proportions of the constituent elements Fe, Cu, Nb, Si and B varies on either side of the nominal composition have been used for this study.

2. Experimental details

Amorphous FeCuNbSiB ribbons, (10 mm in width and 30 μm in thickness) with actual composition displayed in table 1 were prepared by the single-roller melt-quenching technique. The actual composition of the amorphous ribbons was determined by inductively coupled plasma optical emission spectroscopy and energy dispersive absorption of x-rays (EDAX) analysis. For convenience, the samples are henceforth designated by their Fe concentration. The samples were sealed in glass ampules filled with 5 N purity argon after repeated evacuation and flushing sequences. All the sample-containing ampoules were placed side by side within the uniform heating zone of the furnace so as to ensure that all the samples received identical heat treatment. In order to promote the growth of nanocrystalline grains in the amorphous matrix during the initial stages of crystallization, the alloy ribbons were annealed at $520\,^{\circ}C$ for fixed durations of time $t_A = 3$, 5, 10, 15 and 20 min. The choice of the annealing temperature was dictated by two main considerations. First, the primary crystallization in these alloys takes

Table 1. Actual composition of the amorphous precursor alloys. The numbers in parentheses show the deviation of the alloy composition from the composition $Fe_{73.5}Cu_1Nb_3Si_{13.5}B_9$.

Sample label	Fe (at.%)	Cu (at.%)	Nb (at.%)	Si (at.%)	B (at.%)
$Fe_{73.26}$	73.26	0.96	3.00	13.08	9.70
	(−0.24)	(−0.04)	(0.00)	(−0.42)	(+0.70)
$Fe_{74.0}$	74.00	1.00	3.00	15.80	6.20
	(+0.50)	(0.00)	(0.00)	(+2.30)	(−2.80)
$Fe_{74.37}$	74.37	0.96	3.02	14.15	7.50
	(+0.87)	(−0.04)	(+0.02)	(+0.65)	(−1.50)
$Fe_{74.60}$	74.6	1.00	3.00	15.00	6.40
	(+1.1)	(0.00)	(0.00)	(+1.50)	(−2.60)
$Fe_{74.78}$	74.78	0.92	2.63	15.3	6.30
	(+1.28)	(0.00)	(−0.38)	(+1.8)	(−2.70)

place around [4] 520 °C. Second, a comparison can be sought with the results of a similar study on $Fe_{73.5}Cu_1Nb_3Si_{13.5}B_9$ reported previously [10]. The structure of the nanocrystalline grains was investigated by x-ray diffraction (XRD) and Mössbauer spectroscopy (MS), the morphology by scanning electron microscopy (SEM) and atomic force microscopy (AFM), and the composition by EDAX. These techniques were also used to thoroughly characterize the samples in the amorphous state. Note that the parent amorphous samples were subjected to 'stress-relieving' annealing at 80 °C for 48 h before nanocrystallizing them.

XRD patterns were recorded at room temperature in the step–scan mode with $2\theta = 0.02°$ steps over the range $10° \leqslant 2\theta \leqslant 100°$ on a Philips diffractometer in θ–2θ reflection geometry using Cu Kα radiation. A single run lasted 15 h. Mössbauer spectra were recorded in the transmission geometry at room temperature using a conventional constant-acceleration spectrometer and a 20 mCi ^{57}CoRh source having an intrinsic linewidth (full width at half maximum, FWHM) of 0.28 mm s^{-1}. Typically more than 10^6 counts were accumulated in each channel and the spectrometer was calibrated using α-Fe foil. The quoted isomer shifts are relative to metallic α-Fe at room temperature.

While monitoring the alterations in the XRD patterns and MS spectra brought about by progressive isothermal annealing at 520 °C, discernible changes with respect to the corresponding data taken on the reference amorphous samples could be detected only for annealing times $t_A \geqslant 15$ min. Therefore, only the XRD, MS, SEM, AFM and EDAX data taken on the amorphous precursors and the samples annealed at 520 °C for 20 min (henceforth referred to as the nanocrystalline samples) are reported in this paper.

3. Results and discussion

3.1. XRD patterns

Figure 1 not only compares the XRD patterns of different alloys in the amorphous (a-) state with their nanocrystalline (n-) counterparts but also with the XRD pattern generated for a *bulk crystalline* system in which *three phases*, tetragonal Fe_3B, hexagonal Fe_2Si and cubic Fe_3Si, are simultaneously present in *equal proportion*. Note that (i) for the sake of clarity the frequency of the data points has been reduced by a factor of 2, (ii) the intensity of scattered x-ray photons is in counts per second (cps), (iii) the x-ray intensity data have been corrected for background counts using the empty sample-holder runs taken in the same geometry as that used when the sample is mounted on the sample-holder, and (iv) the intensities of the Bragg peaks in the

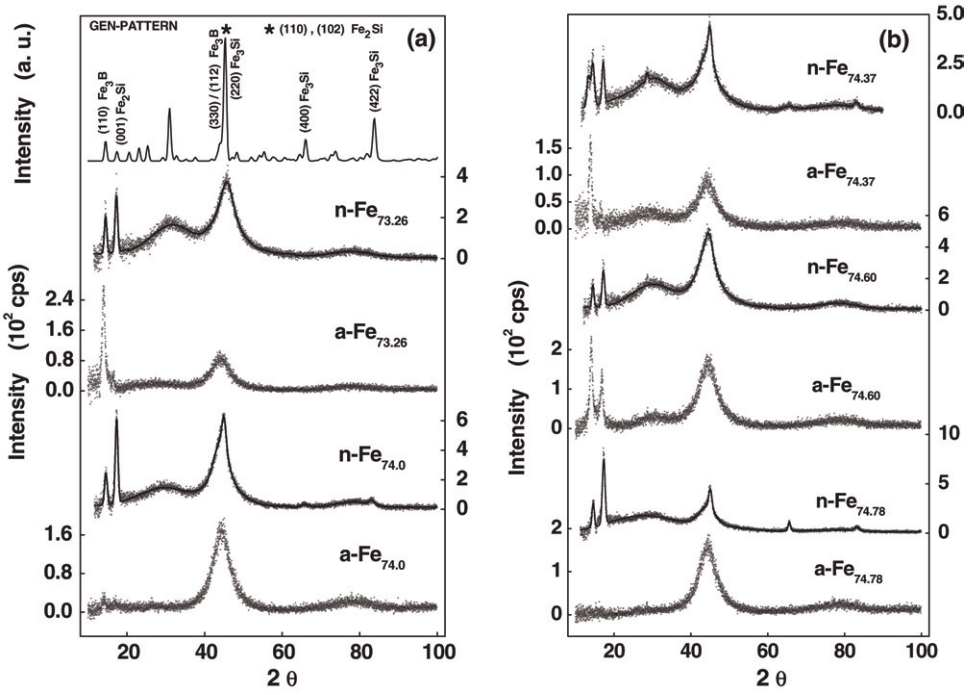

Figure 1. Room temperature x-ray diffraction (XRD) patterns of the amorphous FeCuNbSiB alloys before and after they were annealed at 520 °C for 20 min. The XRD pattern generated for a crystalline system, in which three phases, tetragonal Fe_3B, hexagonal Fe_2Si and cubic Fe_3Si (of DO_3 structure), are simultaneously present, in equal proportion, is included for comparison in the part (a) of the figure.

XRD pattern generated using the relevant space groups reported in the literature [29] must be treated with great caution since the actual atomic positions in the metastable Fe_3B and Fe_2Si phases are not exactly known; only the peak positions are reliable. Even a cursory glance at figure 1 reveals the existence of sharp Bragg peaks of high intensity at $2\theta_B \cong 14.5°$, 17.3° and 44°–45° in all the nanocrystalline samples and additional weak intensity Bragg peaks at $2\theta_B \cong 65.7°$ and 83.3° in the samples n-$Fe_{74.0}$, n-$Fe_{74.37}$ and n-$Fe_{74.78}$. The Bragg peak (peaks) at $2\theta_B \cong 14.5°$ ($2\theta_B \cong 14.5°$ and 17.3°) is (are) present in amorphous precursors a-$Fe_{73.26}$ and a-$Fe_{74.37}$ (a-$Fe_{74.6}$) as well, presumably due to the nucleation of some crystalline phases during the low-temperature (80 °C) annealing. While the Bragg peaks at $2\theta_B \cong 14.5°$ and 17.3° can be unambiguously identified with the (110) and (001) reflections of tetragonal Fe_3B and hexagonal Fe_2Si phases, respectively [29] (note that neither the bcc Fe–Si phase nor the cubic DO_3 Fe_3Si phase, often reported in the literature, exhibits Bragg reflections at $2\theta < 20°$), those at $2\theta_B \cong 65.7°$ and 83.3° do correspond to (400) and (422) reflections of the cubic DO_3Fe_3Si phase [29]. By contrast, the peak at $2\theta_B \cong 44.5°$ can have contributions from (102) and/or (110) reflections of hexagonal Fe_2Si phase, the (330)/(112) reflection of tetragonal Fe_3B phase, the (220) reflection of cubic DO_3Fe_3Si phase and possibly from some of the phases reported [9, 10] for nanocrystalline $Fe_{73.5}Cu_1Nb_3Si_{13.5}B_9$ annealed at $T_A \geqslant 800$ °C and $t_A \geqslant 1$ h.

The best least-squares fits (continuous curves) to the XRD data taken on nanocrystalline samples are obtained by the procedure illustrated in figure 2. At first, the $2\theta_B$ values for all possible crystalline phases (such as orthorhombic or tetragonal Fe_3B, cubic ϵ-FeSi, hexagonal

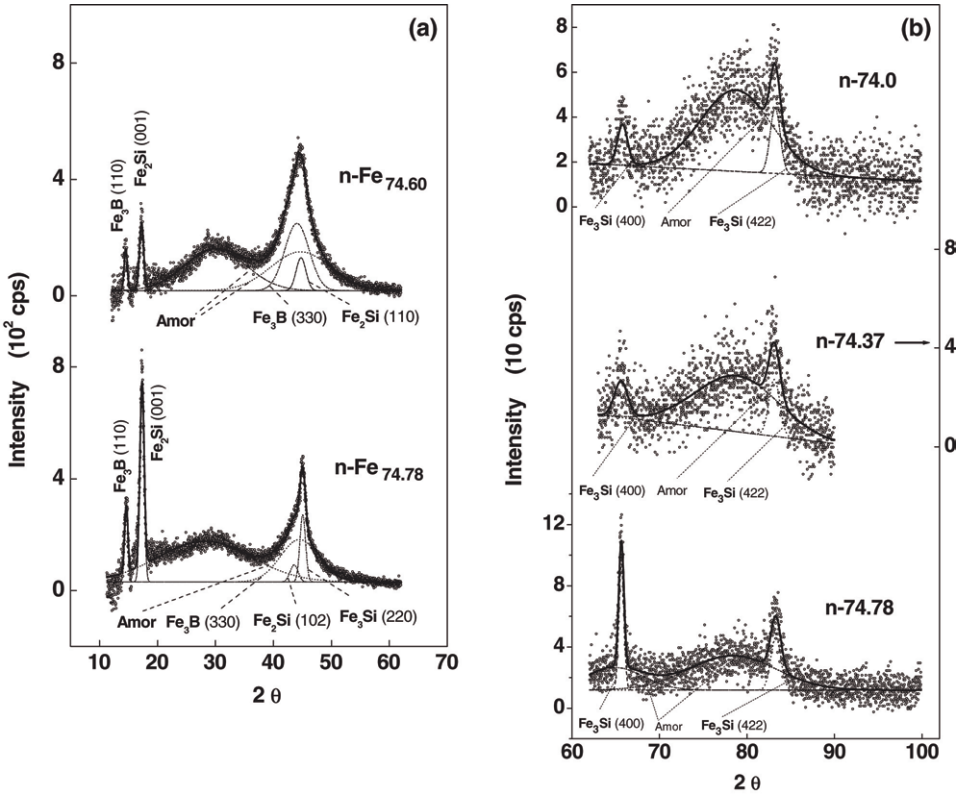

Figure 2. Illustration of the fits to the observed XRD patterns in the angle ranges (a) $10^\circ \leqslant 2\theta \leqslant 62^\circ$ and (b) $62^\circ \leqslant 2\theta \leqslant 100^\circ$ using Lorentzian lineshapes for the Bragg peaks. Extremely broad Lorentzians correspond to the residual amorphous matrix and/or amorphous grain boundary phase whereas the sharper ones represent the Bragg reflections from different (hkl) planes in the nanocrystalline grains of the tetragonal Fe_3B, hexagonal Fe_2Si and cubic DO_3Fe_3Si (actual composition close to $Fe_{80}Si_{20}$) structures, as indicated in the figure.

η-Fe_5Si_3, bcc Fe–Si, cubic DO_3 Fe_3Si, cubic or hexagonal Fe_2Si, orthorhombic or tetragonal $FeSi_2$, orthorhombic FeB, body-centred tetragonal Fe_2B, and fcc $Fe_{23}B_6$) that fall within the 2θ ranges of the observed narrow as well as broad Bragg peaks were collected from the JCPDS cards [29]. Assuming the observed XRD pattern to be a superposition of Lorentzians and using different combinations of the literature [29] $2\theta_B$ values as the starting values for the Lorentzian peak positions, an optimum combination of the *minimum number* of Lorentzians, that closely reproduces the data, was arrived at by the least-squares-fit method. For such fits to be physically meaningful, the minimum number of crystalline phases, besides the amorphous phase represented by extremely broad Lorentzians, should account for all the observed sharp Bragg peaks in a given pattern. This consistency criterion permits us to rule out all the phases mentioned above except for the tetragonal Fe_3B, hexagonal Fe_2Si and cubic DO_3Fe_3Si phases. A typical outcome of this exercise is shown in figure 2. To highlight the quality of the fits on a sensitive scale, the 2θ range covered in the experiments is divided into two segments: $10^\circ \leqslant 2\theta \leqslant 62^\circ$, where sharp Bragg peaks of high intensity occur in all the nanocrystalline samples, and $62^\circ \leqslant 2\theta \leqslant 100^\circ$, where the low-intensity Bragg peaks appear only in n-$Fe_{74.0}$, n-$Fe_{74.37}$ and n-$Fe_{74.78}$. Figure 2 clearly demonstrates the break-up of the fit into the component Lorentzians and their assignment to the relevant Bragg reflections corresponding to a given

Table 2. Peak position ($2\theta_B$), the identified crystalline phase, Miller indices (hkl), lattice parameter (a or c) and average grain size (d) for the component Lorentzian Bragg peaks of the fit. The last three rows display the crystalline volume fractions of different nanocrystallites obtained from the integrated intensity ratios.

$Fe_{73.26}$	$Fe_{74.0}$	$Fe_{74.37}$	$Fe_{74.60}$	$Fe_{74.78}$	Remarks
$2\theta_B = 14.50$ $Fe_3B(110)$ $a = 8.626$ Å $d = 25(2)$ nm	$2\theta_B = 14.58$ $Fe_3B(110)$ $a = 8.582$ Å $d = 23(2)$ nm	$2\theta_B = 14.52$ $Fe_3B(110)$ $a = 8.635$ Å $d = 23(2)$ nm	$2\theta_B = 14.52$ $Fe_3B(110)$ $a = 8.614$ Å $d = 25(2)$ nm	$2\theta_B = 14.60$ $Fe_3B(110)$ $a = 8.569$ Å $d = 25(2)$ nm	Tetragonal $Fe_3B(110)$ $a = 8.61(3)$ Å $a = 8.63$ Å[a]
$2\theta_B = 17.25$ $Fe_2Si(001)$ $c = 5.134$ Å $d = 24(2)$ nm	$2\theta_B = 17.34$ $Fe_2Si(001)$ $c = 5.107$ Å $d = 22(2)$ nm	$2\theta_B = 17.21$ $Fe_2Si(001)$ $c = 5.149$ Å $d = 22(2)$ nm	$2\theta_B = 17.25$ $Fe_2Si(001)$ $c = 5.134$ Å $d = 23(3)$ nm	$2\theta_B = 17.34$ $Fe_2Si(001)$ $c = 5.108$ Å $d = 22(3)$ nm	Hexagonal $Fe_2Si(001)$ $c = 5.13(2)$ Å $c = 5.086(3)$ Å[a]
	$2\theta_B = 43.71$ $Fe_2Si(102)$ $a = 4.077$ Å $d = 12(2)$ nm	$2\theta_B = 43.62$ $Fe_2Si(102)$ $a = 4.038$ Å $d = 12(2)$ nm		$2\theta_B = 43.57$ $Fe_2Si(102)$ $a = 4.112$ Å $d = 12(2)$ nm	Hexagonal $Fe_2Si(102)$ $a = 4.07(4)$ Å $a = 4.052(2)$ Å[a]
$2\theta_B = 44.69$ $Fe_2Si(110)$ $a = 4.052$ Å $a = 4.052$ Å[a] $d = 10(2)$ nm	$2\theta_B = 45.02$ $Fe_3Si(220)$ $a = 5.690$ Å $d = 16(3)$ nm	$2\theta_B = 45.00$ $Fe_3Si(220)$ $a = 5.693$ Å $d = 17(2)$ nm	$2\theta_B = 44.76$ $Fe_2Si(110)$ $a = 4.046$ Å $a = 4.052$ Å[a] $d = 10(2)$ nm	$2\theta_B = 45.06$ $Fe_3Si(220)$ $a = 5.685$ Å $d = 19(3)$ nm	Cubic DO_3 $Fe_3Si(220)$ $a = 5.689(4)$ Å $a = 5.6533$ Å[a]
	$2\theta_B = 65.82$ $Fe_3Si(400)$ $a = 5.674$ Å $d = 11(3)$ nm	$2\theta_B = 65.53$ $Fe_3Si(400)$ $a = 5.696$ Å $d = 11(3)$ nm		$2\theta_B = 65.61$ $Fe_3Si(400)$ $a = 5.686$ Å $d = 20(3)$ nm	Cubic DO_3 $Fe_3Si(400)$ $a = 5.685(11)$ Å $a = 5.6533$ Å[a]
	$2\theta_B = 83.23$ $Fe_3Si(422)$ $a = 5.682$ Å $d = 14(3)$ nm	$2\theta_B = 83.14$ $Fe_3Si(422)$ $a = 5.687$ Å $d = 14(3)$ nm		$2\theta_B = 83.30$ $Fe_3Si(422)$ $a = 5.677$ Å $d = 14(3)$ nm	Cubic DO_3 $Fe_3Si(422)$ $a = 5.682(5)$ Å $a = 5.6533$ Å[a]
Fe_3B-6% Fe_2Si-12%	Fe_3B-4% Fe_2Si-11% Fe_3Si-6%	Fe_3B-4% Fe_2Si-8% Fe_3Si-7%	Fe_3B-4% Fe_2Si-8%	Fe_3B-4% Fe_2Si-12% Fe_3Si-7%	

[a] Reference [26].

crystallographic phase. The quantitative details about the peak positions ($2\theta_B$), Miller indices (hkl) of Bragg reflections, identified crystalline phase, the average nanocrystalline grain size (d) computed using the Scherrer formula, the calculated values of the lattice parameters (c and/or a) and the volume fraction of nanocrystallites (obtained from the ratio of the integrated intensity of a given peak to the total integrated intensity of all the peaks in the XRD pattern) are given in table 2. Note that the above analysis of the XRD patterns has also been carried out by approximating the XRD lineshapes by Gaussian and pseudo-Voigt functions. This comparative study revealed that the Lorentzian function describes the observed lineshapes significantly (marginally) better than the Gaussian (pseudo-Voigt) function but, within the uncertainty limits, the linewidth (and hence the average nanocrystallite size) does not depend on the nature of the function chosen to describe the XRD lineshape.

A close scrutiny of the entries in this table reveals the following. (I) The nanocrystalline grains of the hexagonal Fe_2Si structure manifest themselves as the Bragg reflections (001), (110)/(102) whereas those of the tetragonal Fe_3B structure manifest themselves as the Bragg reflection (110), in all the nanocrystalline samples. Additional reflections (220), (400) and

(422) corresponding to the cubic DO_3Fe_3Si structure, appear in the samples n-$Fe_{74.0}$, n-$Fe_{74.37}$ and n-$Fe_{74.78}$ only. (II) The average nanocrystalline grain size (d) has nearly the same value of 16(4) nm *for all* the three reflections (220), (400), and (422) in Fe_3Si crystalline phase whereas for Fe_3B [Fe_2Si] crystalline phase, d decreases from 24(3) nm [22(3) nm] at $2\theta_B \cong 14.5°$ [17.3°], corresponding to the (110) [(001)] Bragg reflection of Fe_3B [Fe_2Si], to $\cong$2 nm [11(3) nm] at $2\theta_B \cong 44.6°$ [43.5°], where the Bragg reflection (330) [(110)] occurs. (III) The lattice parameters calculated from different Bragg reflections have the values $a = 8.61(3)$ Å for the tetragonal Fe_3B phase, $a = 4.07(4)$ Å, $c = 5.13(2)$ Å for the hexagonal Fe_2Si phase and $a = 5.685(11)$ Å for the cubic DO_3Fe_3Si phase. These values compare favourably with the corresponding literature values [29] of $a = 8.63$ Å, $a = 4.052(2)$ Å, $c = 5.086(3)$ Å and $a = 5.6533$ Å. (IV) The volume fractions of the nanocrystalline grains of Fe_3B, Fe_2Si and Fe_3Si structures, estimated from the fractional areas (i.e., the sum of integrated intensities (areas) of the Bragg peaks corresponding to a given crystalline phase divided by the total integrated intensity of all the peaks, including those belonging to the amorphous matrix, in the measured XRD pattern), averaged over all the nanocrystalline samples, turn out to be ≈5%, 10% and 7%, respectively; the remaining 78% volume fraction pertains to the residual amorphous phase plus the amorphous grain-boundary phase between the nanocrystalline grains. The actual volume fractions of the nanocrystalline grains in a given sample are displayed in the last row of table 2. (V) Extremely broad Lorentzians account for the residual amorphous phase and/or amorphous grain-boundary phase. Considering that x-rays probe larger depths in a sample as the diffraction angle 2θ increases, the above stated observation (II) implies that the average size of Fe_3B and Fe_2Si nanocrystalline grains decreases with the depth whereas it is insensitive to changes in depth for Fe_3Si nanocrystalline grains. Alternatively, the observation (II) can be interpreted as indicating that the crystallization of Fe_3B and Fe_2Si grains starts at the surface and then proceeds to the bulk whereas the crystallization of Fe_3Si gets initiated in the bulk itself. The observation of Fe_3B or Fe_3B plus Fe_2Si nanocrystalline grains at both the surfaces (i.e., at low angles) in 'stress-relieved' amorphous precursor ribbons supports this inference. In view of the linear reduction [30] in the lattice parameter from $a = 5.7036$ Å at 12.75 at.% Si to $a = 5.6266$ Å at 31.04 at.% Si in the cubic DO_3 Fe–Si phase, the presently determined range of lattice parameter values $a = 5.674$–5.696 Å corresponds to a range of 15–20 at.% in the silicon content in the so-called Fe_3Si nanocrystalline grains. The range of the silicon content and the average grain size of $d = 16(4)$ nm concur well with the previously reported values of 16–22 at.% Si and $d = 10$–20 nm for the DO_3Fe_3Si phase in FINEMET alloys of similar composition. However, our results are at variance with the findings of all the previous studies where either the cubic DO_3Fe_3Si phase or the bcc Fe–Si phase alone was detected or where Fe_3Si nanocrystalline grains are claimed to fill nearly 40% of volume during the initial 10 min of annealing at 520 °C in nanocrystalline $Fe_{73.5}Cu_1Nb_3Si_{13.5}B_9$. By contrast, the crystallization kinetics in the present case is extremely sluggish and completely different crystalline phases, namely tetragonal Fe_3B and hexagonal Fe_2Si, (apart from the cubic DO_3Fe_3Si phase in some samples) are formed during the initial stages of crystallization ($t_A \leqslant 20$ min) at the same annealing temperature.

3.2. Mössbauer spectra

'Zero-field' ^{57}Fe Mössbauer spectra (open circles) taken at room temperature on amorphous FeCuNbSiB alloys before and after they have been annealed at 520 °C for 20 min are shown in the figure 3 along with the optimum fits (continuous curves) obtained using the modified version of the Hesse and Rübartsch method [31] due to Le Caer and Dubois [32]. In this method, a linear correlation between the *local* isomer shift, δ, and the *local* magnetic hyperfine

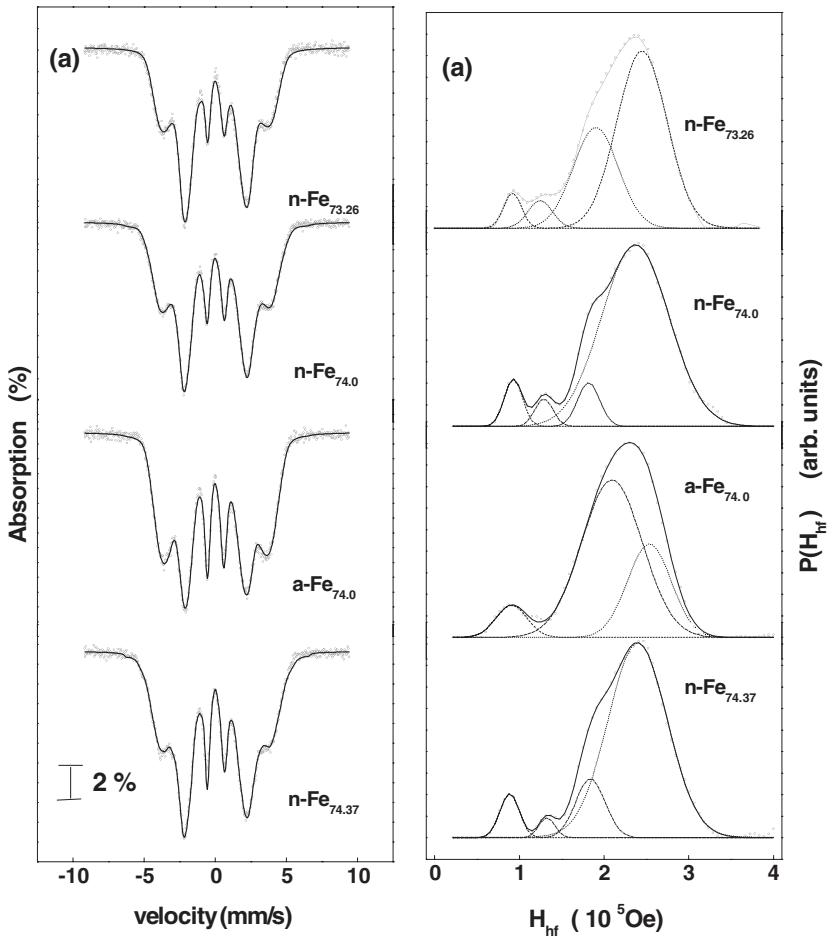

Figure 3. Room-temperature ^{57}Fe Mössbauer spectra (open circles) along with the best fits (continuous curves) obtained by the Le Caer–Dubois method for the amorphous FeCuNbSiB alloys before and after annealing them at 520 °C for 20 min are shown in ((a)(a)). The magnetic hyperfine field distributions corresponding to the best fits, denoted by closed circles, are shown in ((b)(b)) along with the component Gaussian distributions and their resultant distribution (continuous curves through closed circles).

field, $H_{\rm hf}$, of the type

$$\delta(H_{\rm hf}) = \delta(H^o_{\rm hf}) - \alpha(H_{\rm hf} - H^o_{\rm hf}) \tag{1}$$

is used to reproduce the observed asymmetry in the Mössbauer lines, and the intensity ratio, b (defined as $I_{1,6}{:}I_{2,5}{:}I_{3,4} = 3{:}b{:}1$), full width at half maximum (FWHM) of the subspectral lines, Γ, isomer shift, δ, quadrupole splitting, Δ, and the coefficient α in equation (1) are varied to achieve the best least-squares fits to the observed Mössbauer spectra. Since the hyperfine parameters, $H_{\rm hf}$, δ and Δ, and the shapes of their distributions are not known *a priori* and the Mössbauer spectra for the nanocrystalline samples (with the exception of n-$Fe_{74.78}$) do not differ too much from those of their amorphous counterparts, the Le Caer–Dubois method [32] was used to arrive at the optimum values for the average intensity ratio, $\overline{b}$, the mean hyperfine field, $\overline{H}_{\rm hf}$ (listed in table 3), and the probability distribution of the magnetic hyperfine fields, $P(H_{\rm hf})$ (denoted by closed circles in figure 3), for the

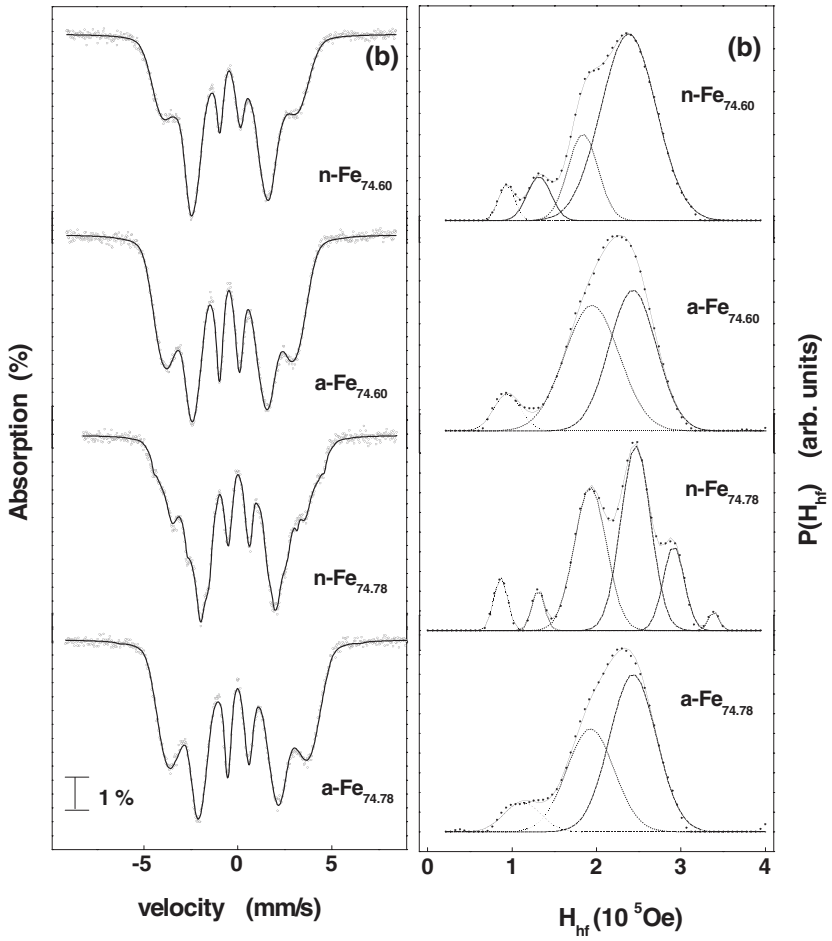

Figure 3. (Continued.)

entire Mössbauer spectrum without making any distinction between the amorphous and nanocrystalline samples. Evidently, $P(H_{\rm hf})$ comprises a minimum of three (four) Gaussian distributions in the amorphous (nanocrystalline, barring n-$Fe_{74.78}$) samples. To ascertain whether or not the component Gaussian distributions actually describe the measured Mössbauer spectra, individual Mössbauer spectra (each consisting of six Lorentzian-shaped lines) were calculated at discrete $H_{\rm hf}$ values (2 kOe apart) along the abscissas of the $P(H_{\rm hf})$ versus $H_{\rm hf}$ Gaussian-shaped curves and added to form a resultant pattern for comparison with the experimental Mössbauer spectrum. Such a fit was indistinguishable from the one obtained previously by the method [32] which does not assume any particular shape for $P(H_{\rm hf})$. In the case of n-$Fe_{74.78}$, six subspectra (corresponding to different Fe sites which can occur in Fe_2Si and within the range of Si concentrations between [33] 10 and 25 at.% in Fe–Si alloys with the DO_3 structure), in addition to the amorphous subspectrum, had to be included in order to achieve the best agreement with the measured Mössbauer spectrum. The above procedure yielded the optimum average values for hyperfine field, $\overline{H}_{\rm hf}^{\rm sub}$, Γ, and δ for the subspectra displayed in table 3, and demonstrated that the average quadrupole splitting, Δ, is negligibly small in all the samples (amorphous and nanocrystalline) in that the inclusion or exclusion of Δ in the analysis has practically no influence on the quality of fits.

Table 3. Hyperfine parameters corresponding to the main Mössbauer spectra and subspectra for different amorphous and nanocrystalline samples.

Sample/phase/sites		$\overline{H}_{\rm hf}^{\rm sub}$	Γ (kOe)	δ (kOe)	$\overline{H}_{\rm hf}$ (mm s^{-1})	$\overline{b}$ (kOe)	$\langle\theta\rangle$
	Amorphous						
Sample	Phase						
$Fe_{74.0}$	Amor	91(2)	37(2)	0.18	214.0	2.34	59°
	Amor	209(7)	72(6)	0.10			
	Amor	253(4)	52(5)	0.07			
$Fe_{74.6}$	Amor	94(2)	32(2)	0.18	210.0	2.40	60°
	Amor	201(7)	70(5)	0.10			
	Amor	246(3)	54(3)	0.07			
$Fe_{74.78}$	Amor	97(4)	23(5)	0.18	214.0	2.37	60°
	Amor	125(5)	28(6)	0.16			
	Amor	199(7)	62(7)	0.10			
	Amor	247(4)	53(3)	0.07			
	Nanocrystalline						
Sample	Phase						
$Fe_{73.26}$	Amor	92(2)	22(1)	0.18	217.0	3.81	81°
	Amor + Fe_2Si (I)	127(2)	30(2)	0.16			
	Amor + Fe_2Si (II)	187(2)	49(2)	0.11			
	Amor + Fe_3B	242(2)	61(1)	0.07			
$Fe_{74.00}$	Amor	93(1)	21(1)	0.18	221.4	3.21	71°
	Amor + Fe_2Si (I)	129(1)	22(2)	0.16			
	Amor + Fe_2Si (II)	182(1)	26(2)	0.12			
	Amor + Fe_3B	237(2)	80(1)	0.08			
$Fe_{74.37}$	Amor	89(2)	22(1)	0.18	221.2	2.37	77°
	Amor + Fe_2Si (I)	133(1)	19(3)	0.15			
	Amor + Fe_2Si (II)	184(1)	35(2)	0.11			
	Amor + Fe_3B	240(2)	70(1)	0.07			
$Fe_{74.6}$	Amor	93(1)	20(1)	0.18	214.5	3.90	84°
	Amor + Fe_2Si (I)	132(1)	28(2)	0.15			
	Amor + Fe_2Si (II)	184(2)	35(1)	0.11			
	Amor + Fe_3B	238(2)	69(2)	0.07			
$Fe_{74.78}$	Amor	86(1)	19(1)	0.18	220.3	3.99	88°
	Amor + Fe_2Si (I)	130(1)	18(1)	0.16			
	Amor + Fe_2Si (II)	192(1)	45(1)	0.11			
	Amor + Fe_3Si (A_4)	200(1)	59(1)	0.10			
	Amor + Fe_3B + Fe_3Si (A_5)	245(1)	34(1)	0.07			
	Fe_3Si (A_6)	286(2)	31(1)	0.05			
	Fe_3Si (D + A_7 + A_8)	316(1)	12(1)	0.02			

In table 3, the subspectra corresponding to different $\overline{H}_{\rm hf}^{\rm sub}$ values for nanocrystalline grains are attributed to different non-equivalent Fe sites in the Fe_2Si (e.g. I and II), Fe_3B and DO_3 Fe–Si structures according to the procedure illustrated below for the DO_3 structure. The DO_3 structure in the stoichiometric compound Fe_3Si consists of two different Fe sites [34]: D-sites have 8 nearest-neighbour (nn) Fe atoms while A-sites have 4 Fe and 4 Si nearest neighbours. For Si concentrations in Fe–Si alloys in the range 10–25 at.%, Fe atoms on the D-sites still have 8 nn Fe atoms but those at A-sites have varying number of nn Fe or Si atoms depending on the Si concentration. In table 3, A_n denotes that an Fe atom on A-site has n nearest-neighbour Fe atoms. Thus, in the sample n-$Fe_{74.78}$, the values of $\overline{H}_{\rm hf}^{\rm sub} \simeq 200$, 245, 286,

and 316 kOe correspond to $n = 4$, 5, 6 and $D + A_7 + A_8$, respectively. These values of $\overline{H}_{hf}^{sub}$ are in excellent agreement with those reported previously [5–11, 15–21, 24] for the DO_3 structure of nanocrystalline grains in FINEMET. However, contrary to the earlier reports, the Mössbauer spectra for all the nanocrystalline samples (including n-$Fe_{74.78}$), in the present case, have substantial contributions arising from two non-equivalent Fe sites in the Fe_2Si structure, the lone Fe site in the Fe_3B structure and different Fe atom locations in the residual amorphous matrix; e.g., $\overline{H}_{hf}^{sub} = 130(3)$ and 187(5) kOe, $\overline{H}_{hf}^{sub} = 241(4)$ kOe and $\overline{H}_{hf}^{sub} = 91(3)$, 130(3), 185(5) and 240(4) kOe, for Fe_2Si, Fe_3B and amorphous matrix, respectively. In the n-$Fe_{74.78}$ sample, these contributions are in addition to those arising from the DO_3 structure. Annealing leaves the average hyperfine field $\overline{H}_{hf}^{sub} = 91(3)$ kOe essentially unaltered but significantly reduces the higher values of $\overline{H}_{hf}^{sub}$ compared to those in the precursor amorphous state. The reduced $\overline{H}_{hf}^{sub}$ indicates that the amorphous matrix is depleted of Fe to some extent as a result of the formation of the nanocrystalline grains. Furthermore, consistent with the XRD result that nanocrystalline grains of Fe_2Si and Fe_3B are present in the amorphous sample a-$Fe_{74.60}$ but not in the samples a-$Fe_{74.0}$ and a-$Fe_{74.78}$ (figure 1), $\overline{H}_{hf}^{sub}$ values, close to those found in the Fe_2Si and Fe_3B structures, appear only in a-$Fe_{74.60}$ and not in a-$Fe_{74.0}$ and a-$Fe_{74.78}$ (table 3).

The intensity ratio b, by virtue of its definition

$$b = 4\sin^2\theta/(1+\cos^2)\theta \tag{2}$$

in terms of the angle θ between the γ-ray and *local* magnetic hyperfine field (or *local* magnetic moment) directions, provides useful information about the local-spin arrangement. According to equation (2), for a perfectly random alignment of the local magnetic moments (spin-glass order), $b = 2.0$, whereas b assumes the limiting values 0 and 4 when all the moments are aligned *parallel* ($\theta = 0°$) and *perpendicular* ($\theta = 90°$) to the γ-ray direction, respectively. The average intensity ratio, $\overline{b}$, therefore, reflects the average orientation of the magnetic moments. Equation (2), when rewritten in the form

$$\langle\cos^2\theta\rangle = (4-b)/(4+b) \qquad \text{or} \qquad \langle\sin^2\theta\rangle = 2b/(4+b), \tag{3}$$

yields the value for the average angle $\langle\theta\rangle$, corresponding to the observed values of $\overline{b}$, displayed in table 3. In equation (3), $\langle\ \rangle$ denotes the average over the distribution of the angle θ. The calculated values of $\langle\theta\rangle$ indicate that the magnetic moments in the amorphous samples point, on average, 40° out of the ribbon plane whereas the magnetic moment in the nanocrystalline grains plus the residual amorphous matrix point, on average, 2° to 19° out of the ribbon plane depending on the Fe concentration in the nanocrystalline samples. The orientation of the magnetic moments is decided by the outcome of the competition between different types of magnetic anisotropies: mainly stress and shape anisotropies in the amorphous case as against magneto-crystalline, stress and shape anisotropies in the nanocrystalline case.

3.3. Scanning electron microscopy (SEM), atomic force microscopy (AFM) and energy dispersive absorption of x-rays (EDAX) analysis

Figures 4 and 5 depict the scanning electron micrographs and atomic force micrographs (in the dynamic force mode) taken on the *ribbon surface* for the samples a-$Fe_{73.26}$, (typical of other amorphous samples too), n-$Fe_{73.26}$, n-$Fe_{74.6}$, (representative of the samples n-$Fe_{74.0}$ and n-$Fe_{74.37}$ as well) and n-$Fe_{74.78}$. In these micrographs, the nanocrystalline grains of the hexagonal Fe_2Si, tetragonal Fe_3B and cubic DO_3Fe_3Si structures should appear as grains of needle or rod-like or ellipsoidal shape, slightly elongated objects and cuboids or spheres, respectively. Consistent with the XRD and Mössbauer results, these micrographs clearly reveal the existence of nanocrystalline grains mostly of needle or rod-like or ellipsoidal shape and occasionally

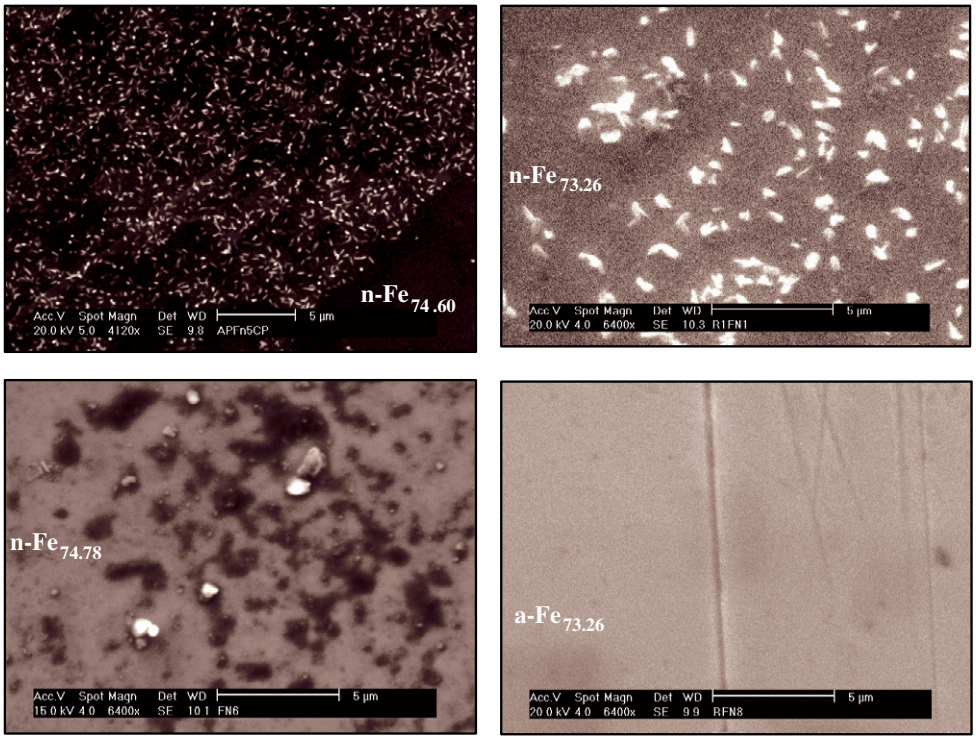

Figure 4. Scanning electron micrographs of the ribbon surface for the samples a-$Fe_{73.26}$, n-$Fe_{73.26}$ and n-$Fe_{74.6}$ (which are representative of the other samples too), and for the nanocrystalline sample n-$Fe_{74.78}$ which exhibits a completely different nanostructure.

of slightly elongated shape in all the nanocrystalline samples except for n-$Fe_{74.78}$, in which grains of spherical shape are observed. In conformity with the XRD data, needle or rod-like or ellipsoidal as well as slightly elongated nanocrystalline grains have also been observed in such micrographs taken in certain regions of the amorphous ribbon of the samples of a-$Fe_{73.26}$, a-$Fe_{74.37}$, a-$Fe_{74.6}$ only; no such regions exist in a-$Fe_{74.0}$ and a-$Fe_{74.78}$ samples. The average size of 30(5) nm for the nanocrystalline grains of the Fe_2Si or Fe_3B structures and 25(5) nm for the nanocrystalline grains of the cubic DO_3 structure obtained from the atomic force micrographs also conform well with the corresponding values deduced from the XRD data. Furthermore, the spot evaluation of composition by the EDAX analysis at ten different locations in the nanocrystalline samples where the scanning electron micrographs display the highest density of nanocrystalline grains revealed that the composition of most of the needle or rod-like grains is close to Fe_2Si in all the nanocrystalline ribbons with the exception of n-$Fe_{74.78}$, in which the spherical nanocrystalline grains have a composition close to $Fe_{80}Si_{20}$. The compositional analysis by EDAX over an area of 50 μm square of the residual amorphous matrix showed only a slight reduction in the Fe and Si concentrations relative to their values in the precursor amorphous state, presumably due to a very small crystalline volume fraction in the present case.

In the passing, it should be mentioned that annealing the amorphous precursors in question at 560 °C for 1 h yields results that are in agreement with those reported previously so far as the formation of a majority DO_3Fe_3Si-like phase is concerned but differ in the persistence of Fe_2Si and Fe_3B phases as minor phases.

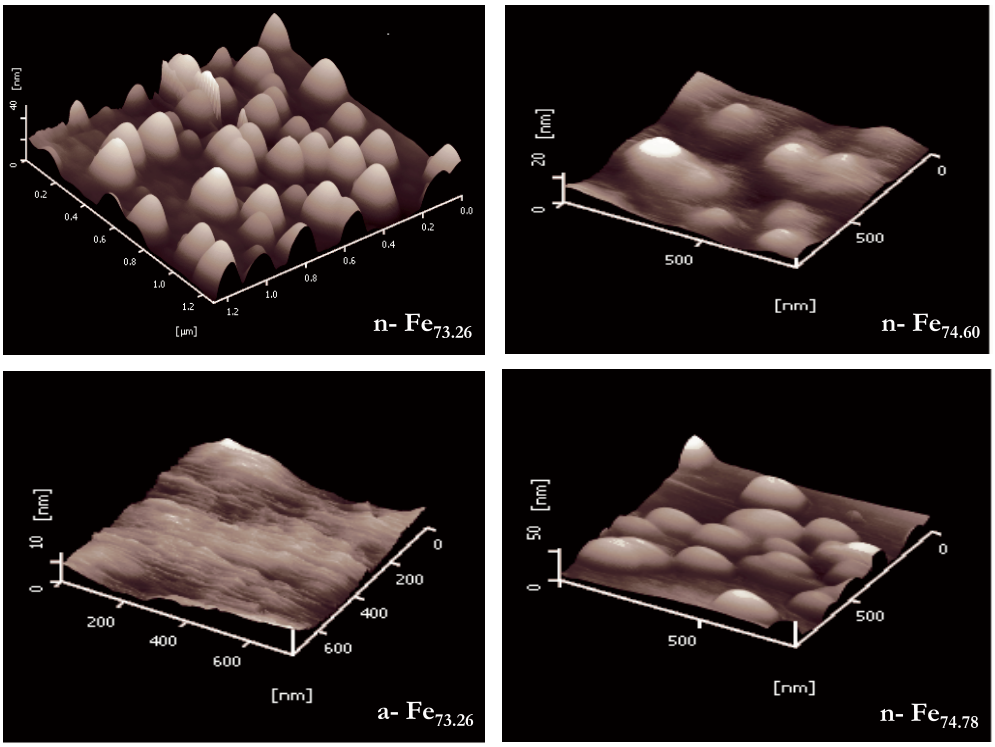

Figure 5. Atomic force micrographs (taken in the dynamic force mode) of the ribbon surface for the samples a-$Fe_{73.26}$, n-$Fe_{73.26}$, n-$Fe_{74.6}$ and n-$Fe_{74.78}$.

4. Summary and conclusion

The structure and composition of crystalline phases formed during the initial stages of crystallization were investigated by XRD, Mössbauer spectroscopy (MS), SEM, AFM and EDAX in amorphous precursor alloys with the concentrations of the constituents Fe, Cu, Nb, Si, and B varying around the composition $Fe_{73.5}Cu_1Nb_3Si_{13.5}B_9$ (extensively studied in the literature) which were subjected to annealing at 520 °C for time durations t_A in the range 3 min $\leqslant t_A \leqslant$ 20 min. XRD and MS results reveal the existence of new crystalline phases, tetragonal Fe_3B and hexagonal Fe_2Si, in all the nanocrystalline samples studied besides the well-known cubic Fe–Si phase with the DO_3 structure, which occurs only in the samples n-$Fe_{74.0}$, n-$Fe_{74.37}$ and n-$Fe_{74.78}$. Detailed analysis of XRD patterns strongly indicates that the crystallization of Fe_3B and Fe_2Si nanocrystalline grains starts at the surface and then proceeds to the bulk whereas the crystallization of Fe_3Si gets initiated in the bulk itself. The lattice parameters determined for the phases Fe_3B, Fe_2Si and Fe_3Si from the XRD data are in very good agreement with the literature values, and the average grain sizes of Fe_3B, Fe_2Si and Fe_3Si nanocrystallites deduced from the XRD data using the Scherrer formula conform well with those determined from AFM measurements. The XRD results also yield the volume fractions of the nanocrystalline grains of the Fe_3B, Fe_2Si and Fe_3Si structures as ≈5%, 10%, and 7%, respectively, and a Si concentration in the range 15–20 at.% in the Fe_3Si nanocrystalline grains. EDAX analysis confirms that the composition of nanocrystalline grains in all the FINEMET alloys (in the n-$Fe_{74.78}$ sample, in particular) is close to Fe_2Si (Fe_3Si). The observation that the amorphous alloy with the least Nb concentration yields the highest volume

fraction of nanocrystalline grains of the Fe_3Si structure seems to indicate that the reduction in the Nb concentration promotes nanocrystalline growth. This inference is in agreement with the conclusions drawn by Miglierini and co-workers [15, 16] from a systematic study of the effect of the variation in Nb concentration on the crystallization kinetics in FINEMET alloys. Mössbauer data reveal that the magnetic moments in the amorphous precursors point, on average, 40° out of the ribbon plane and that, in the nanocrystalline alloys, this angle varies between 2° and 19° depending on Fe concentration. This result, in particular, has a direct bearing on the nature of magnetic anisotropy and its influence on the soft magnetic properties.

Acknowledgments

This work was supported by the Department of Science Technology, New Delhi, under grant No. SR/S5/NM-04/2003. The authors thank Professor C Bansal for permitting the use of the Mössbauer spectrometer.

References

[1] Yoshizawa Y, Oguma S and Yamauchi K 1989 *J. Appl. Phys.* **64** 6044
[2] Yoshizawa Y and Yamauchi K 1990 *Mater. Trans. JIM* **31** 307
[3] Herzer G 1989 *IEEE Trans. Magn.* **25** 3327
Herzer G 1990 *IEEE Trans. Magn.* **26** 1397
[4] Kotaoka N, Inoue A, Masumoto T, Yoshizawa Y and Yamauchi K 1989 *Japan. J. Appl. Phys.* **28** L1820
[5] Kohmoto O, Haneda K and Choh T 1990 *Japan. J. Appl. Phys.* **29** L1460
[6] Fujinami M, Hashiguchi Y and Yamamoto T 1990 *Japan. J. Appl. Phys.* **29** L477
[7] Zemčik T, Jirásková Y, Závěta K, Eckert D, Schneider J, Mattern N and Hesske D 1991 *Mater. Lett.* **10** 313
[8] Jiang J, Aubertin F, Gonser U and Hilzinger H R 1991 *Z. Metallk.* **82** 698
[9] Rixecker G, Schaaf P and Gonser U 1992 *J. Phys.: Condens. Matter* **4** 10295
[10] Hampel G, Pundt A and Hesse J 1992 *J. Phys.: Condens. Matter* **4** 3195
[11] Pulido E, Navarro I and Hernando A 1992 *IEEE Trans. Magn.* **28** 2424
[12] Herzer G 1992 *J. Magn. Magn. Mater.* **112** 258
[13] Zhou X Z, Morrish A H, Naugle D G and Pan R 1993 *J. Appl. Phys.* **73** 6597
[14] He K Y, Sui M L, Liu Y and Zhao B F 1994 *J. Appl. Phys.* **75** 3684
[15] Miglierini M 1994 *J. Phys.: Condens. Matter* **6** 1431
[16] Sitek J, Lipka J, Miglierini M and Toth T 1995 *J. Magn. Magn. Mater.* **140–144** 441
[17] Garcia del Muro M, Zquiak R, Batlle X and Parellada J 1998 *J. Magn. Magn. Mater.* **140–144** 475
[18] Zhu J, Clavaguera N, Clavaguera-Mora M T and Howells W S 1998 *J. Appl. Phys.* **84** 6565
[19] Garitaonandia J S, Schmool D S and Barandiaran J M 1998 *Phys. Rev.* B **58** 12147
[20] Grenéche J M, Miglierini M and Slawska-Waniewska A 2000 *Hyperfine Interact.* **126** 27
[21] Crisan O, Grenéche J M, Le Breton J M, Crisan A D, Labaye Y, Berger L and Filoti G 2003 *Eur. Phys. J.* B **34** 155
[22] Noth T H, Lee M B, Kim H J and Kang I K 1990 *J. Appl. Phys.* **67** 5568
[23] Sawa T and Takahashi Y 1990 *J. Appl. Phys.* **67** 5565
[24] Ponpandian N, Narayanasamy A, Chattopadhyay K, Manivel Raja M, Ganesan K, Chinnasamy C N and Jeyadevan B 2003 *J. Appl. Phys.* **93** 6182
[25] Rahman I Z, Kamruzzaman Md and Rahman M A 2004 *Phys. Status Solidi* c **1** 3632
[26] Majumdar B and Akhtar D 2005 *Bull. Mater. Sci. (India)* **28** 395
[27] Yoshizawa Y and Yamauchi K 1990 *Mater. Sci. Eng.* A **133** 176
[28] Herzer G 1997 *Handbook of Magnetic Materials* vol 10 ed K H J Buschow (Amsterdam: Elsevier Science) p 415
[29] 1999 *JCPDS Metals and Alloys Data Book*
[30] 1942-1944 *The International Union of x-ray Crystallography. Structure Report* vol 9, p 61
[31] Hesse J and Rübartsch A 1974 *J. Phys. E: Sci. Instrum.* **7** 526
[32] Le Caer G and Dubois J M 1979 *J. Phys. E: Sci. Instrum.* **12** 1083
[33] Stearns M B 1963 *Phys. Rev.* **129** 1136
[34] Cowdery S J and Kayser F X 1979 *Mater. Res. Bull.* **14** 91